



Simulation of particle deposition in a channel with multi-vibrating elastic ribbons

Ehsan Mehrabi Gohari¹ · Ataallah Soltani Goharrizi²

Received: 28 October 2023 / Revised: 29 March 2024 / Accepted: 8 April 2024
© The Author(s) under exclusive licence to OWZ 2024

Abstract

This paper presents a computational study on the flow field, particle trajectory and deposition in a rectangular channel which includes multi-vibrating elastic ribbons mounted on different places of the channel. The diameter of particles varies between 10 μm and 40 μm . Two different places of a vibrating ribbon and four different places of multi-vibrating ribbons are considered. To compare, a fixed ribbon is also considered. Fluid flow equations are solved numerically based on the finite element method. The trajectory of particles was obtained by solving the equation of particle motion that included the inertial, viscous drag and gravity forces. The fluid–structure interaction was considered using an arbitrary Lagrangian–Eulerian method. Detailed analysis of the fluid velocity field and fluid–structure interaction is carried out to investigate the effect of vibrating ribbons on particle deposition. The results were compared with the available experimental and numerical data, and the accuracy of approach was evaluated. Results show that behind the vibrating ribbon, multiple vortices of different sizes are formed, which causes changes in the velocity gradient and flow fluctuations of the upstream and increases the percentage of particle deposition in that area compared to a fixed ribbon. For one ribbon cases, an increase in deposition efficiency is observed when the vibrating ribbon is mounted on the upper wall, and for multi-vibrating ribbon cases, this increase is also observed, but the percentage of deposition is lower than single-ribbon cases. In addition, increasing the diameter of particles and decreasing the Young's modulus increase the deposition percentage of particles.

Keywords Vibrating elastic ribbons · Deposition · Fluid–structure interaction · Young's modulus · Particles

1 Introduction

The study of aerosol and small-size particle motion, deposition and those behaviors is an important issue in many industries and also has many applications, such as air pollution and air pollution control equipment. Cyclones, settling chambers and scrubbers are air pollution equipment that obtaining the particle behavior in that equipment could be very important for those designing. Studying the behavior of particles on some equipment that has a moving piece also has some challenges, because these moving pieces could affect fluid behavior and velocity distribution. The motion and deposition of small-sized particles are under the effect

of fluid velocity distribution. In this case, for simulation, the moving mesh methods should be used for obtaining the fluid and particle motions. In some cases, the fluid that passes over an obstacle could deflect the obstacles based on its structure modulus, such as its Young's modulus; therefore, the particle deposition on these obstacles is affected by those deflections. In the FSI (fluid–structure interaction) method, the effect of fluid on structure deflection or motion is studied. The deflection or motion of a solid structure is due to pressure or stress forces that are exerted by the fluid on the solid. Therefore, the particle in fluid should be deposited on a moving or deflecting solid. A method that is used for modeling fluid on a moving obstacle in a moving mesh system is the ALE (arbitrary Eulerian–Lagrangian method) method. In this method, the solid velocity in a cell is subtracted from the fluid velocity. Many investigators did a lot of work on solid motion and deposition on fixed obstacles in tubes or channels, but investigations on particle deposition on moving objects are relatively rare. In the following, we review some

✉ Ehsan Mehrabi Gohari
emehrabi@tvu.ac.ir

¹ Department of Mechanical Engineering, Technical and Vocational University (TVU), Tehran, Iran

² Department of Chemical Engineering, Faculty of Engineering, Shahid Bahonar University of Kerman, Kerman, Iran

works on the flow field with obstacles, in continue deposition of particles on fixed solids will be reviewed. Kmietek and Kucaba-Piętal [1] studied the effect of the wall-mounted obstacle on laminar fluid flow at different shapes (triangular and rectangular), and they showed that the increase of Reynolds number values increases the length of the recirculation zone. Błoński et al. [2] studied fluid flow in a rectangular microchannel in the presence of a fixed obstacle numerically and experimentally. They demonstrated that for Reynolds values greater than 10, the deformation of the flow field in the microchannel was observed for fluid flow characterized. Goharrizi, Taheri and Fathikalajahi [3] studied the particle motion and deposition from a turbulent stream around a surface-mounted ribbon. They concluded that the particles are deposited around the ribbon due to inertial impaction and gravity force and the dominant deposition mechanism depends on Stokes and gravity numbers. Li et al. [4] developed a computational scheme for simulating aerosol particle dispersion and deposition in turbulent flows in passages with complex geometry. They used a thermodynamically consistent rate-dependent algebraic stress model to simulate the mean turbulent flow fields. They also evaluated the corresponding capture efficiencies of rectangular and trapezoidal blocks for different particle Stokes numbers and showed that the deposition rate decreases significantly as the shape of the obstruction becomes more streamlined. The turbulent flow and particles deposition in wavy duct flows was studied by Hayatia et al. [5]. They used the v_2 -f turbulence model to simulate the turbulent flow through the wavy channel. In their studies, the instantaneous turbulence fluctuating velocities were simulated using the Kraichnan Gaussian random model. The drag, Saffman lift, Brownian and gravity forces were considered to act on the particle equation of motion. Their results showed that the duct wavy walls significantly increased the particle deposition rate. Ansari et al. [6] obtained the solid particles motion and deposition in a filter with regular and irregular arrangement of blocks using the lattice Boltzmann method. In their study, the flow was considered to be laminar. They concluded that the regular filter has a more deposition efficiency for small particles (less than 15 μm diameters) and an irregular filter is more suitable for filtering large particles (more than 15 μm diameters). Predicting the particle deposition characteristics using a modified Eulerian method on a tilted surface in the turbulent flow was studied by Abdolzadeh, Mehrabian and Goharizi [7]. The v_2 -f turbulence model with a two-phase Eulerian approach was used by these investigators, because the v_2 -f model can accurately calculate the near wall fluctuations which mainly represent the non-isotropic nature of turbulent flow near the walls. In their research, the influence of the tilt angle on the particle deposition rate was investigated. They have shown that considering the turbophoretic force as the only inertia force and neglecting the lift force, leads

to reasonable accuracy in predicting particle deposition rate. Tian and Ahmadi [8] studied the transport and deposition of nano- and microparticles in a turbulent duct flow using different turbulence models. The presented results could provide guidelines for selecting appropriate procedure for simulating nano- and microparticle transport and deposition in various applications. They have shown that when sufficient care was given to the modeling effort, the particle deposition rates could be predicted with reasonable accuracy. A particulate flow in a rib-roughened channel is investigated using LRR model and a Lagrangian method by Andaz and Maso [9]. The LRR turbulence model is a type of the standard Reynolds stress model (RSM) in which six extra transport equations are solved. They used a deflector in the channel to examine its effect on the deposition rate. Their results showed that the deflector increases the deposition rate with different diameter sizes by increasing the interaction between particles and lower channel wall. This study showed that while a deflector increases the particle deposition rate, it can cause pressure drop due to flow blockage. In addition to numerical works, Lai, Byrne and Goddard [10–13] and Kussin and Sommerfeld [14] have experimentally studied the effect of wall roughness on particle deposition. Airborne particle transport and deposition on solid surfaces has an important role in aerosol deposition, infectious diseases transmission and surface soiling. Moving fluids disperse particles by the action of several forces including drag, lift, thermophoresis, buoyancy and Brownian effects. Fabregat and Pallares [15] studied the transport and wall surface deposition of airborne particles in enclosed, buoyancy-driven turbulent flows using fully resolved numerical simulations. They showed that the deposition rate on adiabatic walls is found to be spatially inhomogeneous with particles accumulating near the corners where hot and cold walls meet. They explain these preferential spots by intensified wall-normal turbulent transport in these particular regions. In this study, for the first time, the flow field and particle deposition in a two-dimensional rectangular channel which includes multi-vibrating elastic ribbons have been investigated. Two different places of a vibrating elastic ribbon and four different places of multi-vibrating elastic ribbons are considered. To compare, a fixed ribbon is also considered. Detailed analysis of the fluid velocity field and fluid–structure interaction is carried out to investigate the effect of vibrating elastic ribbons on particle deposition.

2 Geometry and boundary conditions

In this study, 21 geometrical configurations of fluid flow are analyzed including 18 vibrating ribbon geometries (6 vibrating ribbon cases with 3 particle diameters) and 3 fixed ribbon geometries for comparison and validation. The number of

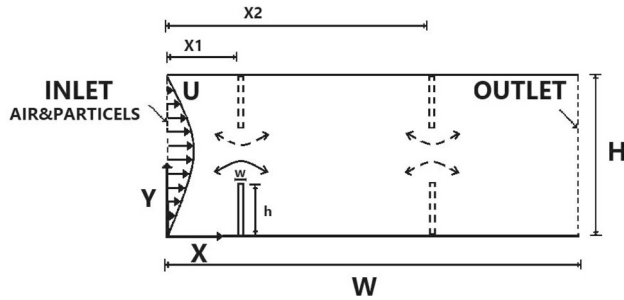


Fig. 1 Schematic representation of a channel

Table 1 Geometric characteristics of the channel and vibrating obstacle

W (mm)	100	h (mm)	10
H (mm)	20	X1(mm)	20
w (mm)	0.2	X2(mm)	60

particles varies between 2000 and 15,950. The diameter of the particles varies between 10 and 40 μm , and their density is considered to be 1000 kg/m^3 . Figure 1 depicts the schematic geometry of the simulated domain, and also information about geometrical characteristics of 19 geometries is presented in Table 1. Moreover, information about geometrical characteristics of 2 fixed geometries that use for validation is the same as the work of May and Clifford [16], Goharrizi et al. [3] and Kmitek and Kucaba [1]. The physical properties of air used in the calculations are $\rho = 1.204 \text{ kg/m}^3$ and $\mu = 1.825 \times 10^{-5} \text{ Pa s}$. The density of the ribbons is considered to be 7850 kg/m^3 , and the Young's modulus of the vibrating ribbons varies between 0.1 and 0.2 Mpa.

For airflow around the ribbons, no slip boundary conditions are assumed over the walls. Zero normal gradients are assumed at the outlet plane. Also, at inlet, a parabolic velocity distribution is considered as follows:

$$U = 0.75 \times Y \times \frac{H - Y}{\left[\frac{H}{2}\right]^2} \quad (1)$$

where U and H are inlet fluid velocity and height of channel, respectively.

3 Computational method

In this study, the flow field and particle deposition in a two-dimensional channel in the presence of one and multi-vibrating elastic ribbons have been investigated. To simulate the airflow as a continuous phase, Navier–Stokes equations are used and it is considered as an incompressible flow due to low air velocity.

$$\rho \nabla \cdot \mathbf{u} = 0 \quad (2)$$

$$\rho \frac{\partial \mathbf{u}}{\partial t} + \rho (\mathbf{u} \cdot \nabla) \mathbf{u} = \nabla \cdot [-p \mathbf{I} + \mathbf{K}] + \mathbf{F} \quad (3)$$

where \mathbf{u} and p are flow velocity and pressure, ρ is the fluid density, μ is the fluid dynamic viscosity, and \mathbf{I} is unit tensor. Also, \mathbf{K} is:

$$\mathbf{k} = (\mu + \mu_T) (\nabla \mathbf{u} + (\nabla \mathbf{u})^T) \quad (4)$$

The well-known standard k - ε turbulence model, which is based on eddy viscosity modeling to Reynolds stress, is used for analysis of flow field. It is a two-equation model that gives a general description of turbulence by means of two transport equations for turbulent kinetic energy and turbulent dissipation rate [17].

The transport equation for turbulent kinetic energy is:

$$\rho \frac{\partial k}{\partial t} + \rho (\mathbf{u} \cdot \nabla) k = \nabla \cdot \left[\left(\mu + \frac{\mu_T}{\sigma_k} \right) \nabla k \right] + P_k - \rho \varepsilon \quad (5)$$

where σ_k is turbulent Prandtl number for k and P_k represents the term kinetic energy production:

$$P_k = \mu_T \left[\nabla \mathbf{u} : (\nabla \mathbf{u} + (\nabla \mathbf{u})^T) \right] \quad (6)$$

The transport equation for the turbulent dissipation rate is:

$$\rho \frac{\partial \varepsilon}{\partial t} + \rho (\mathbf{u} \cdot \nabla) \varepsilon = \nabla \cdot \left[\left(\mu + \frac{\mu_T}{\sigma_\varepsilon} \right) \nabla \varepsilon \right] + C_{1\varepsilon} \frac{\varepsilon}{k} P_k - C_{2\varepsilon} \rho \frac{\varepsilon^2}{k} \quad (7)$$

The turbulent viscosity is calculated by using the following equation:

$$\mu_T = \rho c_\mu \frac{k^2}{\varepsilon} \quad (8)$$

where the five empirical constants of the standard model of turbulence k - ε are C_μ , σ_k , σ_ε , $C_{1\varepsilon}$ and $C_{2\varepsilon}$ with values of 0.09, 1.0, 1.3, 1.44 and 1.92, respectively.

The governing equation in the form of Eq. 2 is discretized into algebraic equations by means of the finite element method [18] by using COMSOL Multiphysics software version 6.1.

Because the vibrating elastic ribbons are moving in time and deform as a function of some parameters (fluid velocity and solid deformation), a deformed mesh (a finite element mesh that will need to change) is employed for the numerical simulation (Fig. 2). The deforming domain feature and deformed geometry interface solve an equation for the mesh

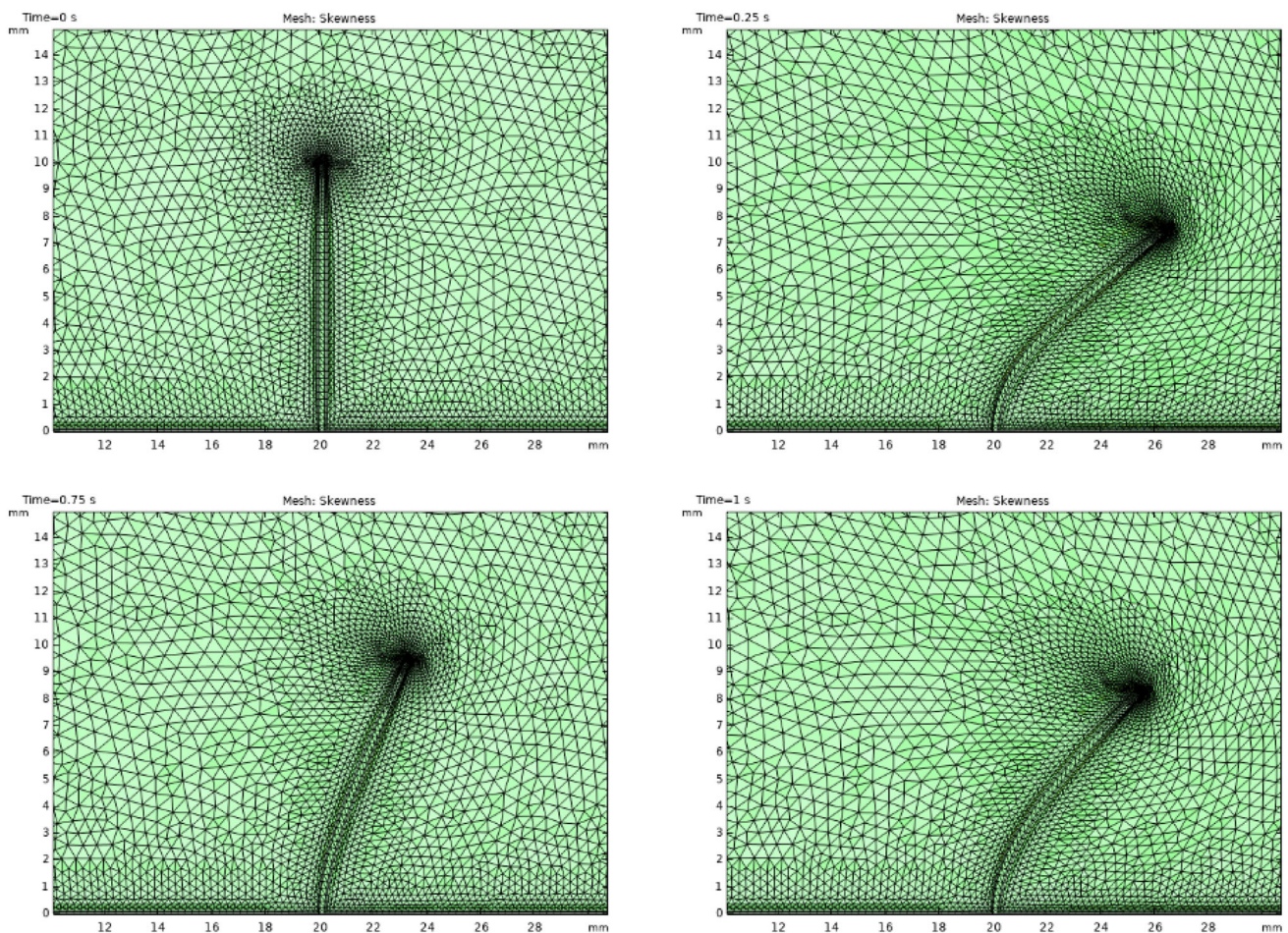


Fig. 2 Deformed grids near the ribbon

displacement. This equation smoothly deforms the mesh given the constraints placed on the boundaries.

There are four types of smoothing methods for computing the deformation of the mesh within each domain Laplace, Winslow, hyperelastic and Yeoh smoothing types. Here, we used Yeoh smoothing. This method generally produces the best results and allows the largest displacement of boundaries before mesh elements become inverted. However, because of its strong nonlinearity, it can cause convergence problems, in particular for time-dependent and segregated solvers [19].

The Yeoh smoothing method is inspired by hyperelastic materials, in this case, the three-term Yeoh hyperelastic model, which is a generalization of a neo-Hookean material, uses a strain energy of the form [19]:

$$w = \frac{1}{2} \int C_1 (I_1 - 3) + C_2 (I_1 - 3)^2 + C_3 (I_1 - 3)^3 + k (J - 1)^2 dV \quad (9)$$

where κ is an artificial bulk modulus, as above, while C_1 , C_2 and C_3 are other artificial material properties. The values of

C_1 and C_3 are 1 and 0, respectively. The value of C_2 controls the nonlinear stiffening of the artificial material under deformation. It is specified in the Stiffening factor field, with a value of 100. The invariants J and I_1 are given by

$$J = \det(\nabla_{X^x}) \quad (10)$$

$$I_1 = J^{-\frac{2}{3}} \text{tr}((\nabla_{X^x})^T \nabla_{X^x}) \quad (11)$$

where x and y are the spatial coordinates of the spatial frame, and X and Y are the reference coordinates of the material frame [19].

The grid is not uniform in the x -direction within the region, with the grid spacing reduced as one moves toward the ribbon wall. There is also no uniform grid region in the y -direction, adjacent to the top edge and a solid boundary under the ribbons. The grid spaces are larger far from the ribbon where the flow is without any considerable variation.

3.1 Particle trajectory

In this study, a Lagrangian description is provided for predicting the trajectory of particles in the fluid. The particle momentum comes from Newton’s law of motion, which states that the net force on a particle is equal to its time rate of change of its linear momentum in an inertial reference frame:

$$m_p \frac{dV}{dt} = \mathbf{F}_D + \mathbf{F}_g + \mathbf{F}_{ext} \tag{12}$$

where \mathbf{F}_D , \mathbf{F}_g and \mathbf{F}_{ext} are drag force, gravity force and any other external force, respectively.

In Eq. 12, drag force, \mathbf{F}_D , is defined as:

$$\mathbf{F}_D = \left(\frac{1}{\tau_p} \right) m_p (\mathbf{u} - \mathbf{v}) \tag{13}$$

where m_p , \mathbf{u} , \mathbf{v} and τ_p are particle mass, particle velocity, fluid velocity and velocity response time, respectively.

A large number of expressions for the particle response time are available; selecting an appropriate drag law requires knowledge of the relative Reynolds number of particles in the flow [20]. The relative Reynolds number of particle is given by the expression

$$Re_r = \frac{\rho \|\mathbf{u} - \mathbf{v}\| d_p}{\mu} \tag{14}$$

where d_p , \mathbf{u} , \mathbf{v} and μ are particle diameter, particle velocity, fluid velocity and fluid viscosity, respectively.

The gravity force is given by:

$$\mathbf{F}_g = m_p \mathbf{g} \frac{(\rho_p - \rho)}{\rho_p} \tag{15}$$

where ρ and ρ_p are fluid and particle density, respectively.

In this study for calculation of the particle trajectories, the Newtonian formulation is used. It defines a set of second-order ordinary differential equations for the components of the particle position based on Newton’s second law of motion. The spherical particles are introduced at a finite number of starting locations with a finite number of particle sizes at each starting location [19].

3.2 Fluid–structure interaction

The fluid–structure interaction (FSI) combines fluid flow with solid mechanics to capture the interaction between the fluid and the solid structure. A solid mechanics interface and a single-phase flow interface model the solid and the fluid, respectively. The FSI couplings appear on the boundaries between the fluid and the solid. The fluid–structure interaction interface uses an arbitrary Lagrangian–Eulerian (ALE)

method to combine the fluid flow formulated using an Eulerian description and a spatial frame with solid mechanics formulated using a Lagrangian description and a material reference frame [21].

As mentioned, the fluid flow is described by the Navier–Stokes equations, which provide a solution for the velocity field \mathbf{u} . The total force exerted on the solid boundary by the fluid is the negative of the reaction force on the fluid,

$$\mathbf{f} = \mathbf{n} \cdot \left\{ -p\mathbf{I} + (\mu (\nabla \mathbf{u} + (\nabla \mathbf{u})^T)) - \frac{2}{3} \mu (\nabla \cdot \mathbf{u}) \mathbf{I} \right\} \tag{16}$$

where p denotes pressure, \mathbf{u} the fluid velocity, μ the dynamic viscosity of the fluid, \mathbf{n} the outward normal to the boundary, and \mathbf{I} the identity matrix.

Because the Navier–Stokes equations are solved in the spatial (deformed) frame, while the structural mechanical interfaces are defined in the material (undeformed) frame, a transformation of the force is necessary. This is done according to

$$\mathbf{F} = \mathbf{f} \cdot \frac{dv}{dV} \tag{17}$$

where dv and dV are the mesh element scale factors for the spatial frame and the material reference frame, respectively.

The coupling in the other direction consists of the structural velocity $\frac{\partial \mathbf{u}_{struct}}{\partial t}$ (the rate of change for the displacement of the structure) which acts as a moving wall for the fluid domain. The spatial frame also deforms with a mesh deformation that is equal to the displacement \mathbf{u}_{struct} of the solid within the solid domains. The mesh is free to move inside the fluid domains, and it adjusts to the motion of the solid walls.

4 Result and discussion

4.1 Validation

To compare our numerical results, a geometry such as the work of May and Clifford [16] and Goharrizi et al. [3] is considered as the Reynolds number equal to 2.5×10^4 . The simulation has been done for different Stokes numbers in the range of 0.05 to 7.3, and the comparison results are presented in Fig. 3.

As can be seen, the results of the present study have acceptable accuracy compared to the experimental and numerical results.

It is worth mentioning the target efficiency of monodisperse aerosol particles is defined as follows:

$$\eta = \frac{\text{rate of particles deposited on the lower wall}}{\text{rate of particles entering the projected area}} \tag{18}$$

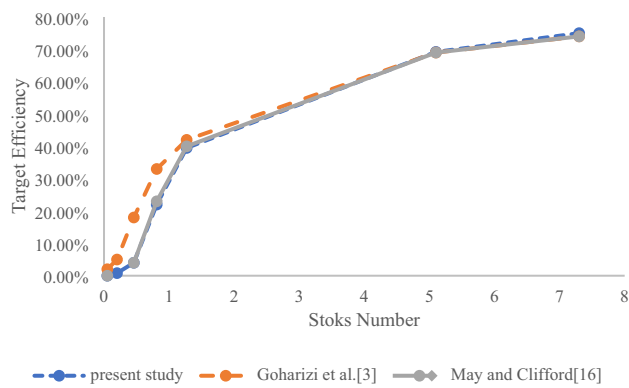


Fig. 3 Comparison between the result of the present study, experimental data of May and Clifford [16] and numerical data of Goharizi et al. (1998) [3] at $Re = 2.5 \times 10^4$

In addition, the simulation was performed for a channel with a fixed ribbon and a Reynolds number of 20. The vortex behind the ribbon can be characterized by the length of the recirculation zone [22]. The length of recirculation was identified as the distance from the ribbon to the vortex closure. Figure 4 presents streamlines in the flow field past a fixed ribbon. The length of the recirculation zone is obtained as 0.152 mm which is in good agreement with the results of Kmittek and Kucaba [1].

4.2 Mesh independency

To determine mesh independency, modeling was done for a channel with one vibrating elastic ribbon mounted on the lower wall in three different types of mesh (Table 2). The number of 2000 particles with a diameter of $20 \mu\text{m}$ and density of 1000 kg/m^3 is considered. Figure 5 shows the average velocity of the ribbon through the channel as a function of time in these cases. As it is observed, the results in the cases where the number of mesh elements is 26,035 or 61,253 are nearly the same, while the difference is large for the case where the number of mesh elements is 4531. Therefore, to obtain more accuracy in results with the minimum computational costs, a finer grid resolution (case 2) is considered.

Fig. 4 Streamlines in the flow field past a ribbon for $Re = 20$

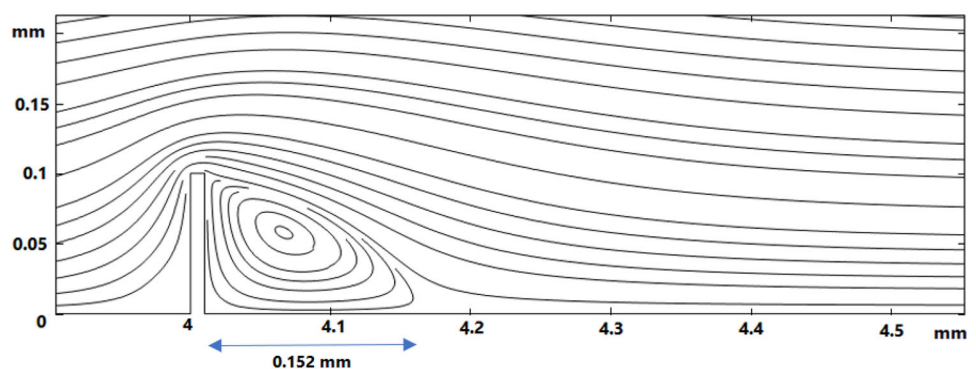


Table 2 Mesh independence study data for the simulated channel

	Number of elements	Average element quality
Normal mesh	4531	0.768
Finer mesh	26,035	0.812
Extra fin mesh	61,253	0.818

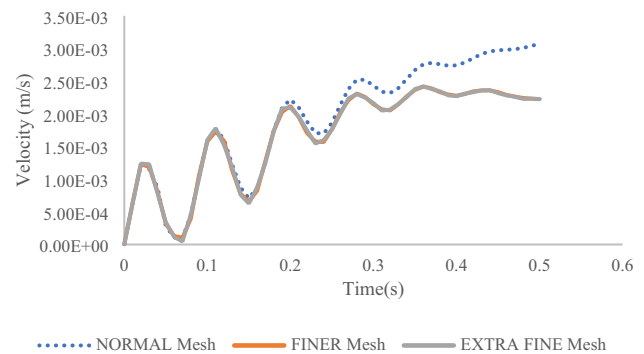


Fig. 5 Average velocity of the ribbon through the channel as a function of time

4.3 One vibrating elastic ribbon

4.3.1 Ribbon on the lower wall

The first model that has been simulated is a channel with the mentioned dimensions (Table 1) containing 15,950 particles with a diameter and density of $40 \mu\text{m}$ and 1000 kg/m^3 , respectively, in such a way that 50 particles are released every 0.025 s for a total duration of 8 s. The density and Young's modulus of the ribbon are considered to be 7850 kg/m^3 and 0.2 Mpa , respectively. It is mounted at 20 mm from the inlet. Meanwhile, the parabolic distribution of the airflow is shown in Eq. 1.

No external force is applied to the vibrating elastic ribbon, and the deformation and vibration of the ribbon occur as a result of air flow. Figure 6 shows streamlines and ribbon

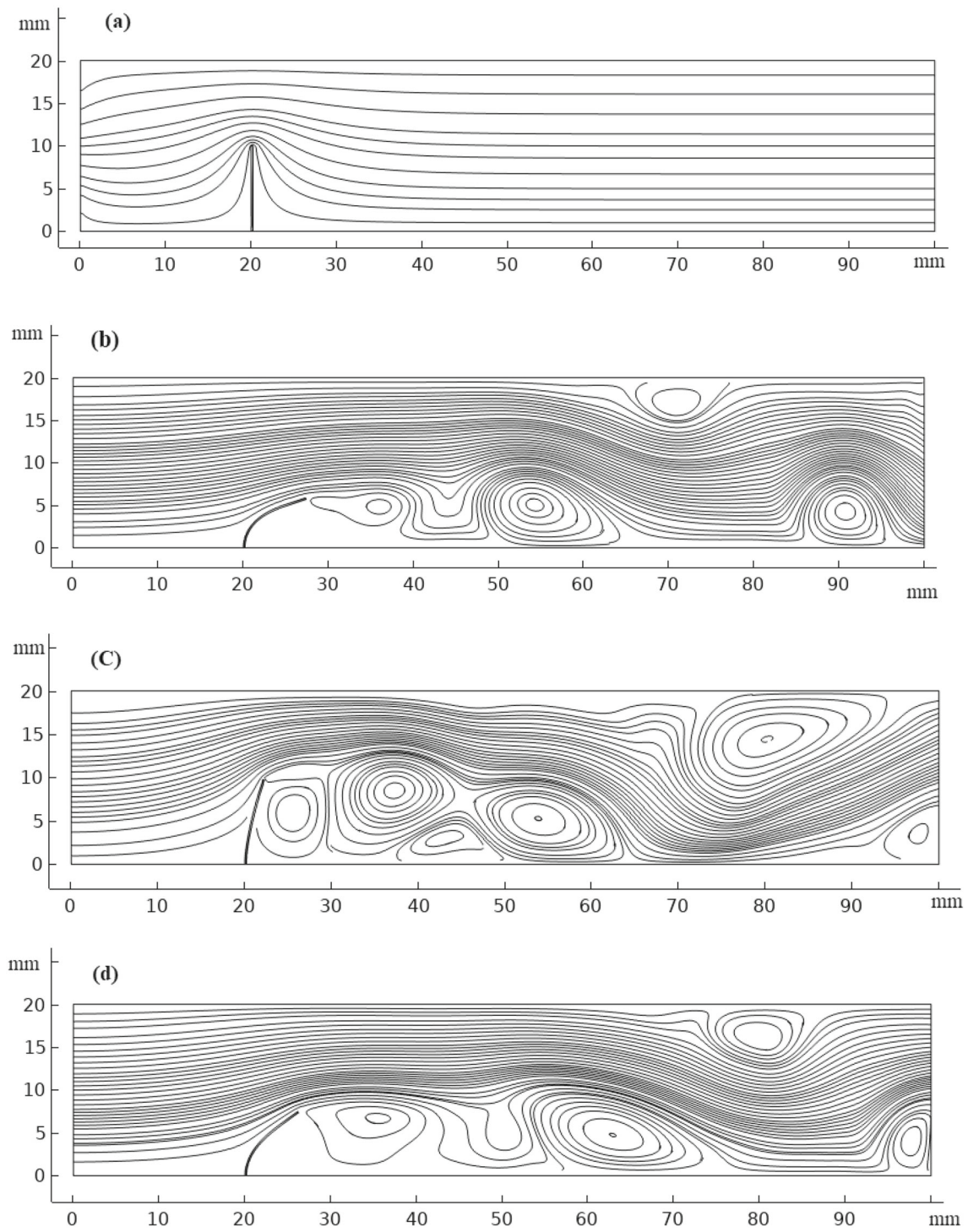
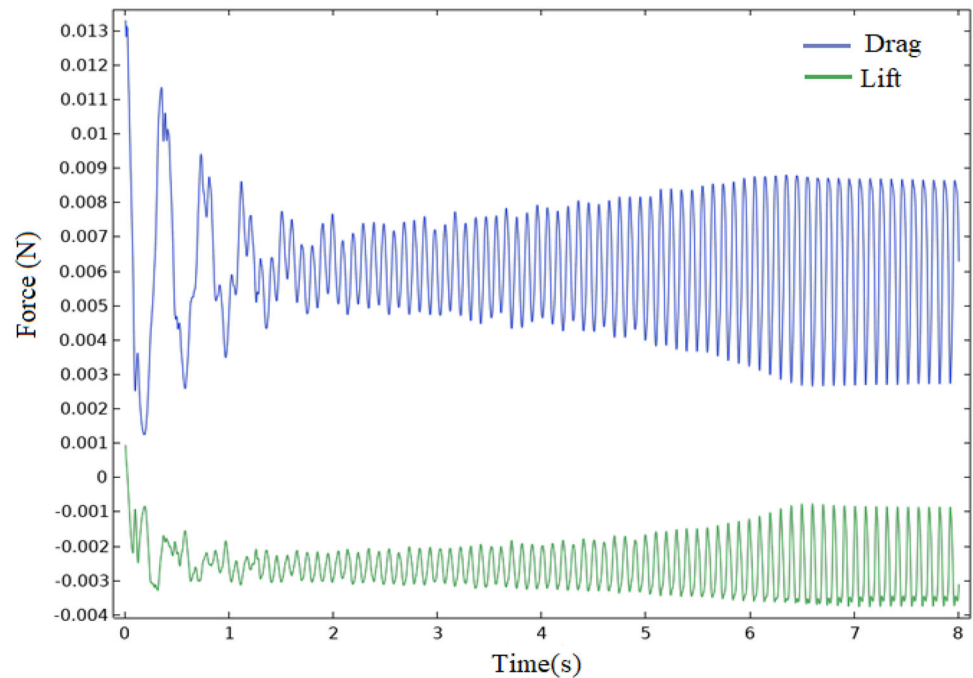


Fig. 6 Streamlines and ribbon deformation over time, when a vibrating ribbon is mounted on the lower wall. **a** $t = 0$ s, **b** $t = 0.2$ s, **c** $t = 0.4$ s, **d** $t = 0.6$ s

Fig. 7 Drag and lift forces versus time



deformation over time, as it is observed at the first (Fig. 6a), the vibrating elastic ribbon is located vertically in the channel, but during the time when the fluid flow passes it, the velocity gradient causes a strong force to be applied to the upper edge of the ribbon and as a result, it inclined to the right (Fig. 6b). Meanwhile, vortices of various sizes are created behind the ribbon which are small at first, but grow over time and the force caused by them causes the elastic ribbon inclined to the reverse direction (Fig. 6c). In the following, the vortices behind the elastic ribbon move downstream, and the force applied by them to the ribbon decreases; therefore, the elastic ribbon inclined to the right again (Fig. 6d). As a result, the elastic ribbon continuously is inclined to the right and left. Figure 7 shows the evolution of the fluid forces over time. Also, the displacement magnitude of elastic ribbon versus time is shown in Fig. 8, as it is observed, that the oscillation of the ribbon is fully developed after $t = 7$ s.

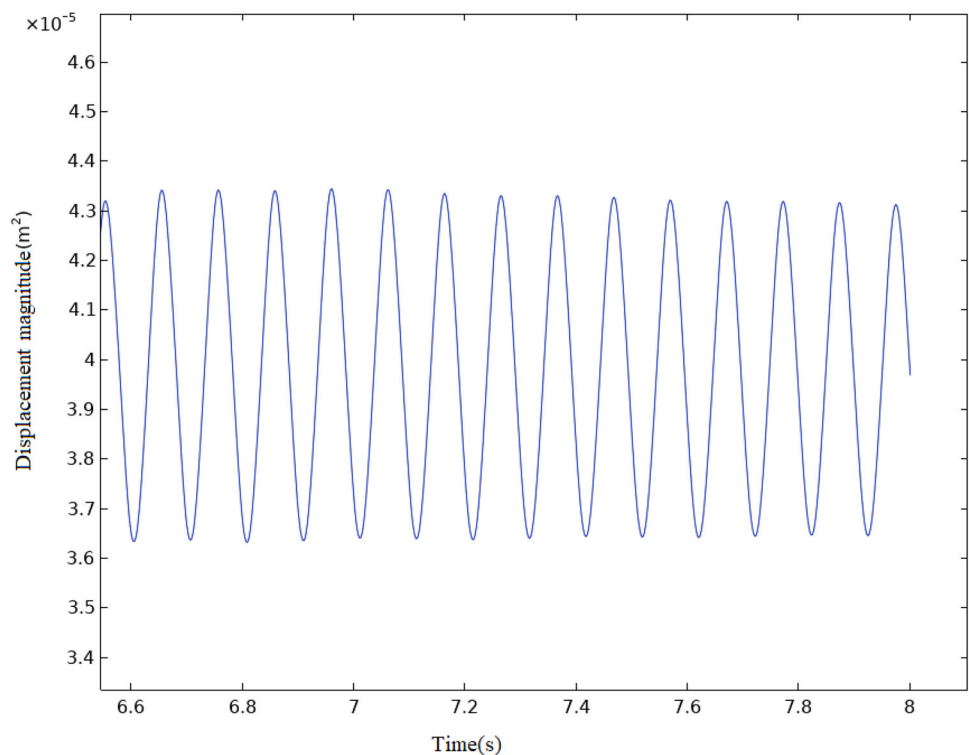
The particle trajectory and velocity contours of the simulated channel are shown in Fig. 9. As it is observed, 15,950 particles in a vertical line are released in a way that 50 particles are released every 0.025 s. At first, due to the initial condition of the fluid flow and the non-slip condition of the channel walls, the particles move in a parabolic shape. During the time when the particles approach the elastic ribbon, due to the velocity gradient and fluid–structure interactions, their direction and velocity change. Therefore, some of them that are at a lower height are deposited at the lower wall of the channel.

The remaining particles, which have less chance of contacting the ribbon, pass over it under the influence of the high

velocity of the flow in that area, and behind the ribbon, they are affected by the created vortices and disperse in the channel. In the following, some of them deposition on the lower wall and some others leave the channel. The amount of particle deposition in downstream depends significantly on the flow conditions and fluid–structure interactions.

To compare, the simulation has also been done for the channel with a fixed ribbon. In the new case, all the specifications are the same as the initial simulation, and the only difference is that the ribbon is fixed and does not move. Results are shown in Table 3. According to this table, for the fixed ribbon case, more particles are deposited upstream (before the ribbon) compared to the vibrating elastic ribbon case, this is because in the fixed ribbon case, the height of the ribbon is fixed and more particles have a chance to collide with it, while in the other case, the ribbon inclined and its height decreases. For the particles that pass over the ribbon, it is vice versa, i.e., the number of particles deposited downstream is more for the vibrating elastic ribbon case. The reason for this phenomenon is that in the vibrating elastic ribbon case, the streamlines behind the ribbon change regularly and multiple vortices of different sizes are formed; as a result, particles affected by these vortices and flow fluctuations have a greater chance to collide with the lower wall.

It should be noted that one of the parameters influencing the vibration of the ribbon is Young's modulus, the decrease in which increases the vibration of the ribbon and flow fluctuations. In order to investigate the effect of this parameter, the simulation for the ribbon with Young's modulus of 0.1 Mpa was also performed. All other specifications are the same as

Fig. 8 Displacement magnitude of a vibrating ribbon versus time

the initial simulation. The results are presented in Table 3. As can be seen, the increase in vibration and flow fluctuations caused an increase in the deposition of particles in the downstream.

4.3.2 Ribbon on the upper wall

One of the most important parameters that affect the motion and deposition of particles in the simulated channel is the location of the vibrating elastic ribbon. Hence, in order to investigate the influence of the location of the vibrating elastic ribbon, the simulation of the ribbon mounted on the upper wall and at a distance of 20 mm from the inlet of the channel was also performed. The diameter of the particles is $40\ \mu\text{m}$. All other specifications are the same as the initial simulation.

The particle trajectory and velocity contours of the simulated channel are shown in Fig. 10. As it is observed, 15,950 particles in a vertical line are released in a way that 50 particles are released every 0.025 s. At first, due to the initial condition of the fluid flow and the non-slip condition of the channel walls, the particles move in a parabolic shape. During the time, due to the force of gravity, the particles tend to move in the vertical direction and toward the lower wall, so the particles that are near the lower wall stick to the wall at the beginning. Also, particles that are at a greater distance from the lower wall move downward due to the force of gravity and the change in flow direction due to the presence of a

ribbon in the upper wall. Therefore, considering that the fluid flow has to move downward to pass the ribbon, it can be said that there is a chance for most of the particles to collide with the lower wall.

One of the other parameters that affect the deposition of particles in the channel is the particle diameter, which shows the significant role of gravitational and drag forces in the deposition process. Hence, in order to investigate the influence of the particle's diameter, the simulated model containing 1000 particles (in a way that 50 particles are released every 0.025 s) with three different diameters of particles, 10, 20, $40\ \mu\text{m}$ is used. Also, in these cases, ribbons are mounted on the upper wall. All other specifications are the same as the initial simulation. Table 4 shows the percentage of particle deposition for these cases. As it is observed, under the same conditions, by increasing the size of the particles, the percentage of particle deposition is also increased. This is because the gravitational forces increase by increasing the density of the particles. More than that, Fig. 11 shows the percentage of deposited particles in a rectangular channel with an elastic ribbon mounted in the upper and lower wall versus diameter. As it is observed, the percentage of deposited particles increases when the elastic ribbon is mounted on the upper wall. This is because in this case, the fluid flow has to move downward to pass the ribbon. Therefore, the chance that particles have a collision with the lower wall increases.

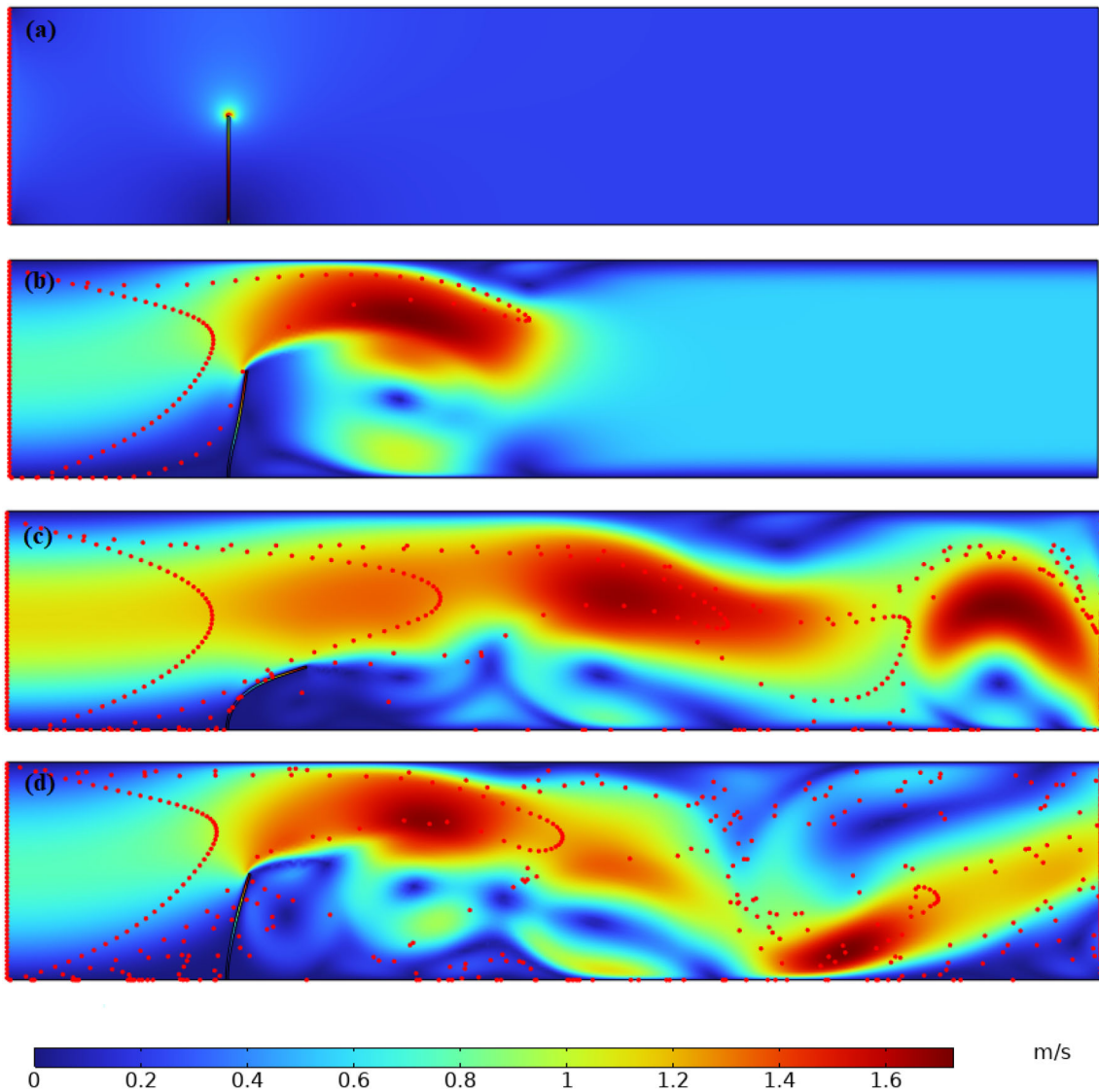


Fig. 9 The particle trajectory and velocity contours for the case with one vibrating ribbon on the lower wall. **a** $t = 0$ s, **b** $t = 0.05$ s, **c** $t = 0.2$ s, **d** $t = 0.4$ s

Table 3 Percentage of deposited particles for a fixed or vibrating ribbon

Cases	Percentage of deposited particles on the lower wall (upstream)	Percentage of deposited particles on the lower wall (downstream)
The fixed ribbon case	20%	10.5%
The vibrating elastic ribbon case	18%	11.26%
The vibrating elastic ribbon case with different Young's modulus	17.8%	13%

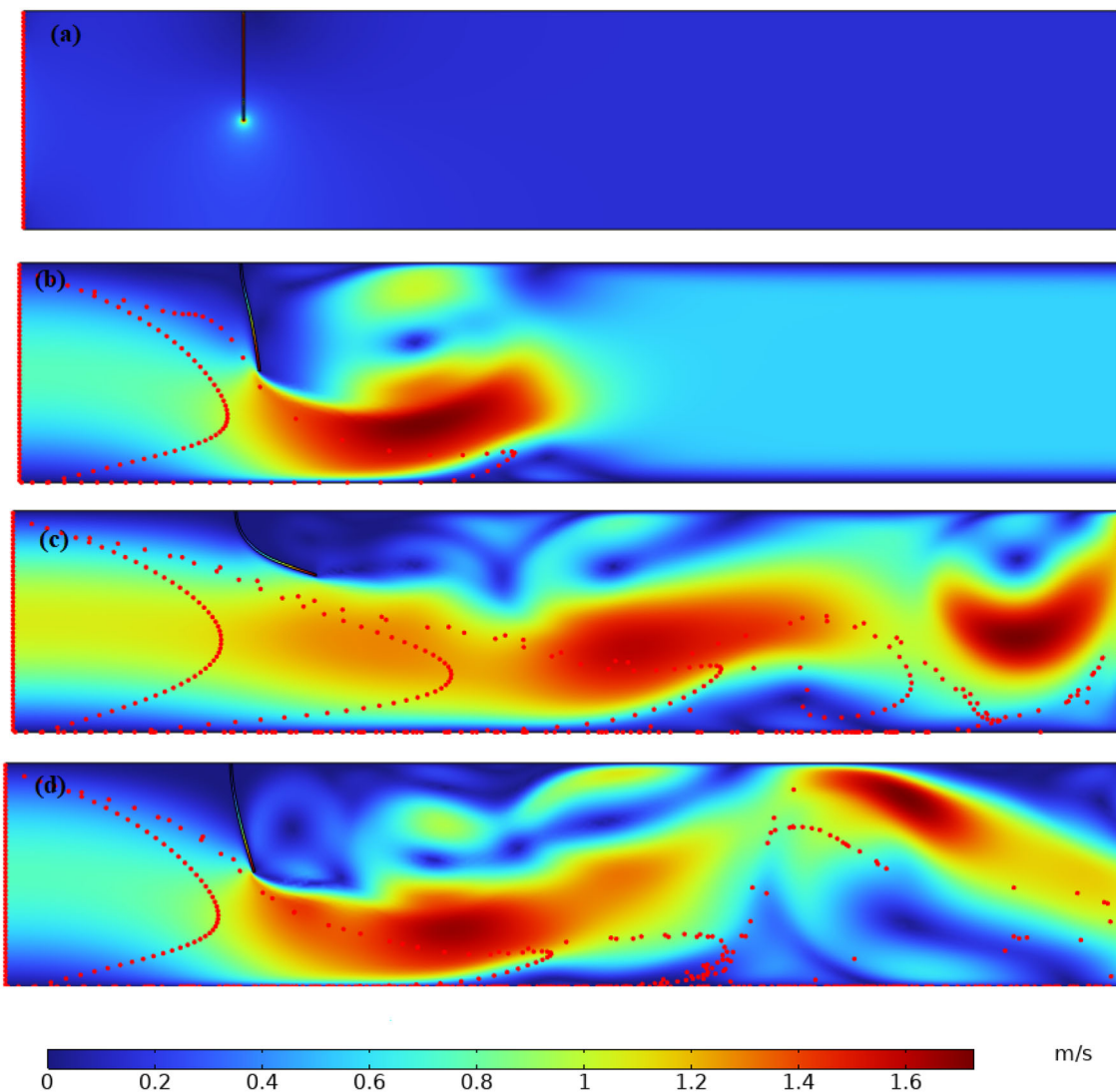


Fig. 10 The particle trajectory and velocity contours, for the case with one vibrating ribbon on the upper wall. **a** $t = 0$ s, **b** $t = 0.05$ s, **c** $t = 0.2$ s, **d** $t = 0.4$ s

Table 4 Percentage of deposited particles in a channel with different diameters of particles

Diameter of particle (μm)	Percentage of deposited particles on the lower wall
10	6.95%
20	18.95%
40	63.68%

4.4 Multi-vibrating elastic ribbons

In order to investigate the effect of multi-vibrating elastic ribbons on the deposition rate of particles, in this research, modeling has been done for a rectangular channel including two elastic ribbons with the same dimensions of height 10 mm and width 0.2 mm, which are mounted at a distance of 20 mm and 60 mm from the inlet.

In addition, in order to investigate the effect of the location of the ribbons, simulation has been done for four different cases. They are both ribbons on the lower wall, both ribbons on the upper wall, the first ribbon on the lower wall and the second on the upper wall and finally, the first ribbon on the upper wall and the second on the lower wall. The diameter of particles varies between 10 and 40 μm . All other specifications are the same as the initial simulation.

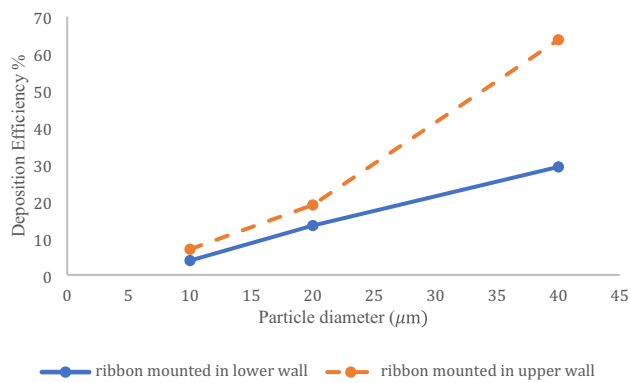


Fig. 11 Deposition efficiency in cases that a ribbon mounted in the lower or upper wall

4.4.1 Two ribbons on the upper or lower wall

Figures 12 and 13 show streamlines and deformation of ribbons over time in the cases of two ribbons on the lower wall and two ribbons on the upper wall, respectively. As it is observed in these cases, similar to the case of the presence of a ribbon on the lower wall, at first the elastic ribbons inclined to the right under the influence of the fluid flow, and then, with the growth and increase in the number of vortices created behind the ribbons, they return to the left.

It should be noted that the moving distance of the second ribbon is different from the first ribbon, which is due to the effect of the presence of the first ribbon on the fluid flow.

The percentage of deposited particles in the cases of two ribbons mounted on the lower wall and on the upper wall is

obtained 22% and 57.4%, respectively. There is a considerable difference between the two values. This is because in the second case, the ribbons increase the chance of particle deposition by changing the direction of fluid flow and particles toward the lower wall of the channel. Figure 14 shows a representation of particles motion with diameters of 10 and 40 μm for the two cases discussed at 0.2 s.

As it is observed under the same conditions, the number of suspended particles with a diameter of 10 μm is more than that of 40 μm, which is the reason, as mentioned, for the effect of gravity.

The percentage of particle deposition for multi-ribbon cases has been compared with single-ribbon cases, and the results are shown in Fig. 15. As can be seen, in single-ribbon cases, the deposition percentage is higher than in multi-vibrating ribbon cases. The reason for this phenomenon is that the presence of a ribbon reduces the cross-sectional area of the channel and, as a result, increases the velocity of the fluid and particles. Now, when the number of these ribbons increases, this increase in velocity occurs at a greater distance from the channel, and therefore, the chance of particle deposition decreases.

4.4.2 One ribbon on the upper and one on the lower wall

In order to compare, the simulation for the cases where two ribbons are on different walls of a channel has been done. Table 5 presents the percentage of particle deposition before and after the ribbon mounted on the lower wall separately. According to Table 5, where the first ribbon is mounted on the upper wall, it has a higher percentage of particle deposition.

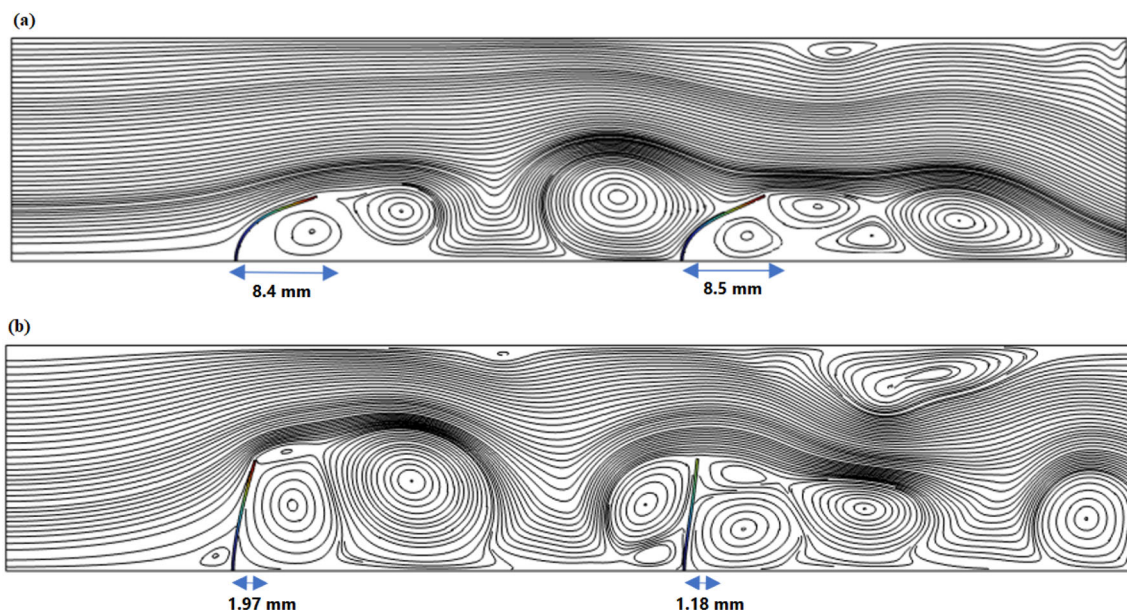


Fig. 12 Streamlines and ribbon deformation over time, when two ribbons are mounted on the lower wall. **a** $t = 0.2$ s, **b** $t = 0.4$ s

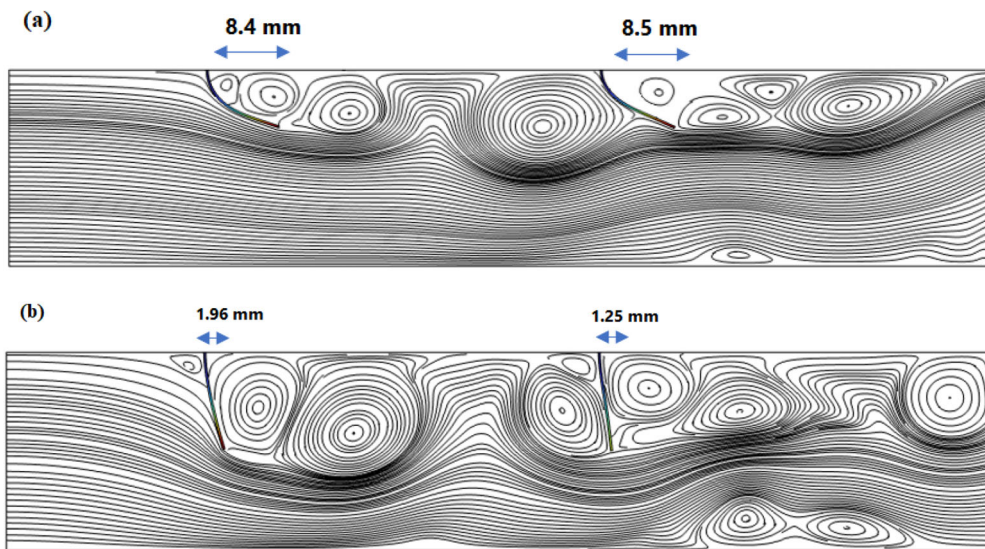


Fig. 13 Streamlines and ribbon deformation over time when two ribbons are mounted on the upper wall. **a** $t = 0.2$ s, **b** $t = 0.4$ s

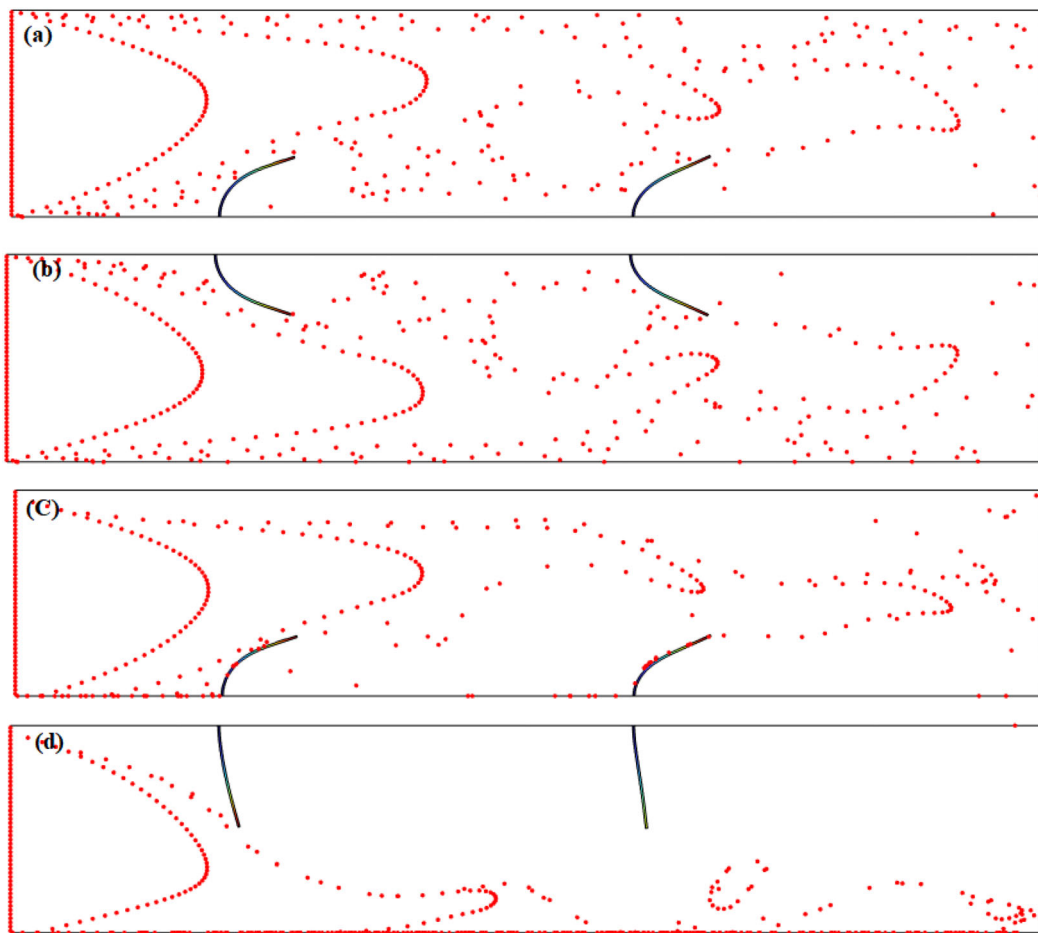


Fig. 14 A representation of particles motion with different diameters at $t = 0.2$ s. **a, b** the diameter of particles is $10 \mu\text{m}$, **c, d** the diameter of particles is $40 \mu\text{m}$

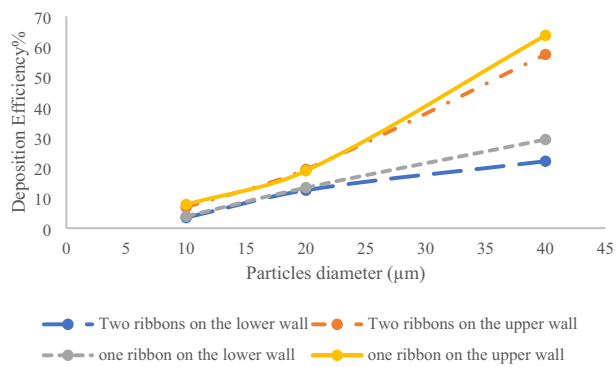


Fig. 15 Comparison of particle deposition percentage for single- and multi-vibrating ribbons cases

Table 5 Percentage of deposited particles for multi-vibrating ribbons mounted on different walls of a channel

Cases with particles diameter = 40 μm	Percentage of deposited particles on the lower wall (upstream)	Percentage of deposited particles on the lower wall (downstream)	Percentage of deposited particles on the lower wall (total)
The first ribbon mounted on upper wall	42.5%	2%	44.5%
The second ribbon mounted on upper wall	18.1%	15.58%	33.68%

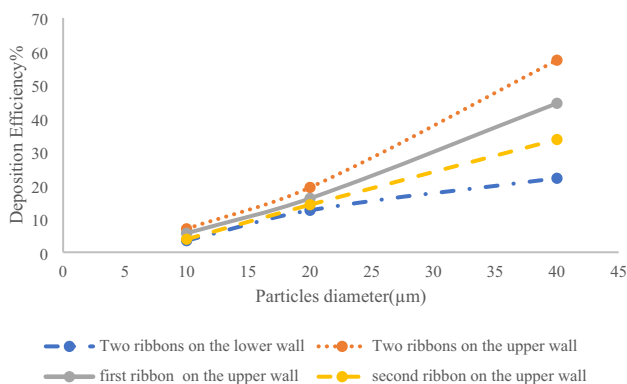


Fig. 16 Deposition efficiency of multi-vibrating ribbons cases

Figure 16 shows the plot of deposition percentage versus particle diameter for all four cases. As it is observed, the highest deposition is related to the case of two ribbons mounted on the upper wall and the lowest is related to the case of two ribbons mounted on the lower wall.

5 Conclusions

The flow field, particle trajectory and deposition of particles in a rectangular channel in the presence of multi-vibrating elastic ribbons were investigated numerically. Two different places of a vibrating elastic ribbon and four different places of multi-vibrating elastic ribbons are considered. To compare, a fixed ribbon is also considered. For obtaining the flow field, the Navier–Stokes equations were solved numerically based on the finite element method (FEM). The trajectory of particles was obtained by solving the equation of particle motion that included the inertial, viscous drag and gravity forces. The fluid–structure interaction (FSI) was obtained by using an arbitrary Lagrangian–Eulerian (ALE) method. The results of the study revealed that the presence of a vibrating ribbon increases the number of particles deposited downstream compared to a fixed ribbon because of multiple vortices of different sizes formed behind the vibrating elastic ribbon. Also, the decrease in the Young’s modulus increases the vibration of the ribbon and flow fluctuations and thus causes an increase in the deposition of particles in downstream. In addition, the result of simulating a channel with an elastic ribbon mounted on an upper wall showed that in this case, deposition efficiency is more than the other cases because of forced change of fluid flow direction toward the bottom wall by the ribbon. More than that, the results of investigating the effect of particle diameter on the percentage of particle deposition showed that the increase in particle diameter due to the increase in gravity increases the percentage of particle deposition. Finally, simulation was done for multi-vibrating ribbons mounted in a rectangular channel in four different cases. The results showed that the highest deposition efficiency is related to the case where the vibrating elastic ribbons are on the upper wall but the percentage of deposition is lower than the case of a single ribbon mounted on the upper wall.

Declarations

Conflict of interest On behalf of all authors, the corresponding author states that there is no conflict of interest.

References

- Kmiotek M, Kucaba-Pietal A (2018) Influence of slim obstacle geometry on the flow and heat transfer in microchannels. *Bull Pol Acad Sci Tech* 66(2):111–118. <https://doi.org/10.24425/119064>
- Błoński S, Domagalski P, Dziubiński M, Kowalewski TA (2011) Hydro-dynamically modified seeding for micro-PIV. *Arch Mech* 63(2):163–182
- Soltani Goharrizi A, Taheri M, Fathikalajahi J (1998) Prediction of particle deposition from a turbulent stream around a surface-mounted ribbon. *Aerosol Sci Technol* 29(2):141–151. <https://doi.org/10.1080/02786829808965559>

4. Li A, Ahmadi G, Bayer RG, Gaynes MA (1994) Particle deposition in an obstructed turbulent duct flow. *J Aerosol Sci* 25(1):91–112. [https://doi.org/10.1016/0021-8502\(94\)90184-8](https://doi.org/10.1016/0021-8502(94)90184-8)
5. Hayati H, Soltani Goharrizi A, Salmanzadeh M, Ahmadi G (2019) Numerical modeling of particle motion and deposition in turbulent wavy channel flows. *Sci Iran* 26(4):2229–2240. <https://doi.org/10.24200/SCI.2019.21405>
6. Ansari V, Soltani Goharrizi A, Jafari S, Abolpour B (2015) Numerical study of solid particles motion and deposition in a filter with regular and irregular arrangement of blocks with using Lattice Boltzmann method. *Comput Fluids* 108:170–178. <https://doi.org/10.1016/j.compfluid.2014.11.022>
7. Abdolzadeh M, Mehrabian MA, Goharizi AS (2011) Predicting the particle deposition characteristics using a modified eulerian method on a tilted surface in the turbulent flow. *Part Sci Technol* 29(3):503–525. <https://doi.org/10.1080/02726351.2010.524975>
8. Tian T, Ahmadi G (2007) Particle deposition in turbulent duct flows—comparisons of different model predictions. *J Aerosol Sci* 38(4):377–397. <https://doi.org/10.1016/j.jaerosci.2006.12.003>
9. Kooh Andaz A, Maso MD (2023) Effect of a deflector on deposition of particles with different diameters in a rib-roughened channel. *Powder Technol* 428:1–12. <https://doi.org/10.1016/j.powtec.2023.118831>
10. Lai ACK, Byrne MA, Goddard AJH (1999) Measured deposition of aerosol particles on a two-dimensional ribbed surface in a turbulent duct flow. *J Aerosol Sci* 30(9):1201–1214. [https://doi.org/10.1016/S0021-8502\(99\)00021-X](https://doi.org/10.1016/S0021-8502(99)00021-X)
11. Lai ACK, Byrne MA, Goddard AJH (2000) Enhanced particle loss in ventilation duct with ribbed surface. *Build Environ* 35(5):425–432. [https://doi.org/10.1016/S0360-1323\(99\)00036-0](https://doi.org/10.1016/S0360-1323(99)00036-0)
12. Lai ACK, Byrne MA, Goddard AJH (2001) Aerosol deposition in turbulent channel flow on a regular array of three-dimensional roughness elements. *J Aerosol Sci* 32(1):121–137. [https://doi.org/10.1016/S0021-8502\(00\)00051-3](https://doi.org/10.1016/S0021-8502(00)00051-3)
13. Lai ACK, Byrne MA, Goddard AJH (2002) Particle deposition in ventilation duct onto three-dimensional roughness elements. *Build Environ* 37(10):939–945. [https://doi.org/10.1016/S0360-1323\(01\)00092-0](https://doi.org/10.1016/S0360-1323(01)00092-0)
14. Kussin J, Sommerfeld M (2002) Experimental studies on particle behavior and turbulence modification in horizontal channel flow with different wall roughness. *Exp Fluids* 33(1):143–159. <https://doi.org/10.1007/s00348-002-0485-9>
15. Fabregat A, Pallarès J (2022) Transport and wall surface deposition of airborne particles in enclosed, buoyancy-driven turbulent flows using fully-resolved numerical simulations. *Int Commun Heat Mass Transf* 134:106048. <https://doi.org/10.1016/j.icheatmasstransfer.2022.106048>
16. May KR, Clifford R (1967) The impaction of aerosol particles on cylinder, sphere ribbons and discs. *Ann Occup Hyg* 10:83
17. Jones WP, Launder BE (1972) The prediction of laminarization with a two-equation model of turbulence. *Int J Heat Mass Transf* 15(2):301–314
18. Liu WK, Li S, Park HS (2022) Eighty years of the finite element method: birth, evolution, and future. *Arch Comput Methods Eng* 29:4431–4453. <https://doi.org/10.1007/s11831-022-09740-9>
19. Renaud CH, Cros JM, Feng ZHQ, Yang B (2009) The Yeoh model applied to the modeling of large deformation contact/impact problems. *Int J Impact Eng* 36(5):659–666. <https://doi.org/10.1016/j.ijimpeng.2008.09.008>
20. COMSOL Multiphysics 6.1 (2022) Particle tracing module user's guide
21. Souli M, Ouahsine A, Lewin L (2000) Prediction of particle deposition from a turbulent stream around a surface-mounted ribbon. *Comput Methods Appl Mech Eng* 190(7):659–675
22. Zhao J, Huang S and Gong L (2014) Numerical studies on geometric features of microchannel heat sink with pin fin structure. In: Paper presented at the 4th microband nano flows conference, UCL, London

Publisher's Note Springer Nature remains neutral with regard to jurisdictional claims in published maps and institutional affiliations.

Springer Nature or its licensor (e.g. a society or other partner) holds exclusive rights to this article under a publishing agreement with the author(s) or other rightsholder(s); author self-archiving of the accepted manuscript version of this article is solely governed by the terms of such publishing agreement and applicable law.